IEEE Access
Multidisciplinary | Rapid Review | Open Access Journal

Received March 30, 2021, accepted April 17, 2021, date of publication April 27, 2021, date of current version May 11, 2021.

Digital Object Identifier 10.1109/ACCESS.2021.3075994

Quadri-Cluster Broadband Circularly-Polarized Sequentially-Rotated Metasurface-Based Antenna Array for C-Band Satellite Communications

NATHAPAT SUPREEYATITIKUL[1], DANAI TORRUNGRUENG[2], (Senior Member, IEEE), AND CHUWONG PHONGCHAROENPANICH[1], (Member, IEEE)

[1]School of Engineering, King Mongkut's Institute of Technology Ladkrabang, Bangkok 10520, Thailand
[2]Research Center of Innovation Digital and Electromagnetic Technology, Department of Teacher Training in Electrical Engineering, Faculty of Technical Education, King Mongkut's University of Technology North Bangkok, Bangkok 10800, Thailand

Corresponding author: Chuwong Phongcharoenpanich (chuwong.ph@kmitl.ac.th)

This work was supported by the King Mongkut's University of Technology North Bangkok under Contract KMUTNB-64-KNOW-12.

ABSTRACT This research proposes a compact quadri-cluster broadband circularly polarized (CP) sequentially-rotated metasurface-based (MTS) antenna array for the C-band frequency spectrum. One cluster of the quadri-cluster MTS-based antenna array consisted of 4 × 4 S-shaped periodically-arranged MTS elements. The sequentially-rotated feed network was utilized to realize circular polarization and improve the impedance bandwidth (IBW), 3-dB axial ratio bandwidth (ARBW) and 3-dB boresight gain bandwidth of the quadri-cluster MTS-based antenna array. Simulations were performed and results were compared with experiments. The measured IBW and ARBW were 84.74% (4.0–9.0 GHz) and 57.6% (4.2–7.6 GHz) at the center frequency of 5.9 GHz, rendering the proposed quadri-cluster MTS-based antenna array suitable for satellite communication applications. In addition, the quadri-cluster MTS-based antenna array achieved the measured 3-dB boresight gain bandwidth of 81.3% (3.9–8.7 GHz), the maximum gain of 10.04 dBic at 5.6 GHz, and low radar cross-section. Specifically, the novelty of this research lies in the use of the sequentially-rotated feed network with the S-shaped MTS elements to effectively enhance ARBW of the quadri-cluster MTS-based antenna array for the C-band frequency spectrum.

INDEX TERMS Antenna array, C-band, circular polarization, metasurface, sequentially-rotated feed network.

I. INTRODUCTION

Circularly polarized (CP) metasurface-based (MTS) patch antennas are commonly used in modern wireless communications, including millimeter wave mobile communications, wireless local area network (WLAN), global navigation satellite systems, satellite communications, and radio frequency identification [1]–[5]. The advantages of CP MTS-based patch antennas include low profile, high gain, and wide bandwidth, vis-à-vis conventional CP patch antennas [6]–[8].

In [9], a dual-microstrip line antenna with 4 × 4 square-shaped MTS elements and cross-slot coupling for WLAN spectrum could achieve an impedance bandwidth (IBW) of 52.5% (1.78–3.05 GHz) and 3-dB axial ratio bandwidth (ARBW) of 31.3% (2.15–2.95 GHz). In [10], a microstrip antenna scheme with MTS structure above asterisk-shaped slot for the L-band spectrum achieved an IBW of 17% (1.4–1.66 GHz) and 3-dB ARBW of 14.5% (1.4–1.62 GHz). A single-fed CP corner-truncated square-shaped MTS-based patch antenna for C-band spectrum achieved an IBW of 45.6% (4.7–7.48 GHz) and 3-dB ARBW of 23.4% (4.9–6.2 GHz) [11]. In [12], a circular patch with slanted-square-slot underneath MTS for C-band spectrum achieved an IBW of 19.7% (6.05–7.33 GHz) and 3-dB ARBW of 16.15% (6–7.05 GHz).

In [13], a planar slot antenna with circular-shaped ground plane underneath corner-truncated square MTS for WLAN spectrum achieved an IBW of 25.7% (3.3–4.2 GHz) and 3-dB ARBW of 11.4% (3.3–3.7 GHz). In [14], a double-slot antenna scheme with 8 × 8 serrated corners-truncated MTS achieved an IBW of 33.33% (8–11.2 GHz) and 3-dB ARBW of 33.33% (8–11.2 GHz). A CP slot antenna with

The associate editor coordinating the review of this manuscript and approving it for publication was Lu Guo.

through-hole MTS for C-band spectrum achieved an IBW of 19.5% (5.1–6.25 GHz) and 3-dB ARBW of 14.9% (5.37–6.25 GHz) [15].

To further enhance CP bandwidths (i.e., IBW and ARBW), antenna arrays have been adopted in the realization of broadband CP MTS-based patch antennas. In [16], 8 × 8 MTS-based antenna array with 16 multi-cascaded split-ring resonators as the feed network for X-band spectrum achieved an IBW of 16% (9.5–10.5 GHz) and 3-dB ARBW of 12% (9.5–10.5 GHz).

In [17], 2 × 2 MTS-based multi-layered antenna array with H-shaped feed network based on substrate integrated waveguide for Q-band spectrum achieved an IBW of 32% (37.4–52.2 GHz) and 3-dB ARBW of 25.8% (39.2–51.5 GHz). In [18], 2 × 2 MTS-based antenna array using 90° branch-line dual-couplers and 180° rat-race single-coupler as the feed network for C-band spectrum achieved an IBW of 49.55% (4.22–7 GHz) and 3-dB ARBW of 28.5% (4.71–6.28 GHz). To simplify the feed network and do away with bulkiness, the sequentially-rotated feed networks were integrated with CP MTS-based antenna arrays to efficiently enhance the IBW, ARBW, and radiation performance [19], [20].

Specifically, this research proposes a compact quadri-cluster broadband CP sequentially-rotated MTS-based antenna array for C-band satellite communications. One cluster of the proposed quadri-cluster CP MTS-based antenna array consisted of 4 × 4 periodically-arranged S-shaped MTS elements [21], and the four clusters of the MTS elements were fed by a sequentially-rotated feed network. Simulations were performed to determine the optimal parameter dimensions, and an antenna prototype was fabricated and experiments carried out to verify the simulation results. In this research, the performance metrics included the IBW, ARBW, 3-dB boresight gain bandwidth, radiation pattern, and radiation efficiency.

The organization of the research is as follows: Section I is the introduction. Section II describes the antenna design, including a single cluster of 4 × 4 S-shaped MTS elements, the sequentially-rotated feed network, and the quadri-cluster MTS-based antenna array scheme. Section III describes the characteristics of the radar cross-section. Section IV details the parametric study and simulation results. Section V discusses the experimental results, and conclusions are provided in Section VI.

II. ANTENNA DESIGN

A. SINGLE CLUSTER OF THE PROPOSED MTS-BASED ANTENNA ARRAY

Figure 1 illustrates the geometry of a single cluster of 4 × 4 S-shaped MTS elements of the quadri-cluster broadband CP sequentially-rotated MTS-based antenna array. The single cluster was fabricated using three layers of FR-4 substrates (upper, middle, and lower) without air gap between substrates. The thickness of the upper (h_1), middle (h_2) and lower substrates (h_3) were 1.6, 1.6, and 0.8 mm. The dielectric

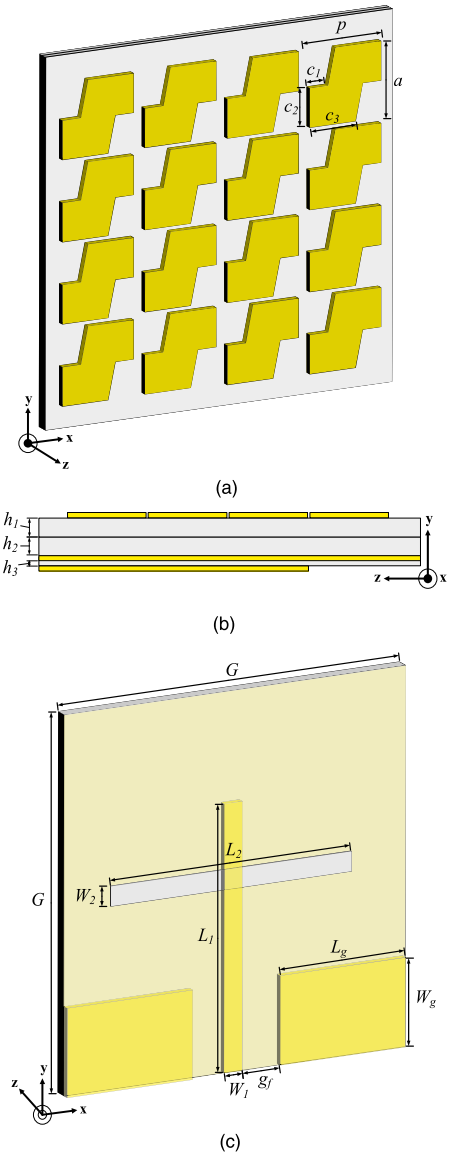

FIGURE 1. Configuration of one single cluster of 4 × 4 S-shaped MTS elements: (a) front view, (b) side view, (c) rear view.

constant (ε_r) and loss tangent ($tan\delta$) of the substrates were 4.3 and 0.025, respectively.

A single cluster consisted of 4 × 4 S-shaped MTS elements periodically arranged on the upper FR-4 substrate. The vertical length of one S-shaped MTS element was 7 mm (a), while the length of the MTS element including voids and the void between two S-shaped MTS elements were 7.4 (p) and 0.4 mm, respectively.

The middle substrate with a rectangular-shaped slot on copper plate functioned as the ground plane. The copper plate was on the rear of the middle substrate. The ground plane and the rectangular-shaped slot were 34 mm × 34 mm ($G \times G$) and 2 mm × 25 mm ($W_2 \times L_2$) in dimension. The lower substrate consisted of a coplanar waveguide (CPW) with a microstrip line and ground. The dimensions of the microstrip line, ground, and gap between the microstrip line and the

TABLE 1. Parameters and optimal dimensions of the quadri-cluster broadband CP sequentially-rotated MTS-based antenna array.

Parameters	W_{sub}	L_{sub}	h_{S1}	h_{S2}	h_{S3}	W_f	L_f	L_a	R	W_s	L_{S1}
Values (mm)	68	68	1.6	1.6	0.8	1.8	34	15	3.5	1.8	13.8
Parameters	L_{S2}	W_1	W_2	W_3	W_4	W_5	W_6	W_7	W_8	W_{gnd}	L_{gnd}
Values (mm)	7.4	1.8	0.4	1.4	0.4	0.6	0.7	0.4	0.7	8	10

ground were 1.8 mm × 24 mm ($W_1 \times L_1$), 8 mm × 12.5 mm ($W_g \times L_g$), and 1.1 mm (g_f), respectively. Simulations were performed using CST Studio Suite.

A single cluster of 4 × 4 S-shaped MTS elements of the quadri-cluster broadband CP sequentially-rotated MTS-based antenna array has been presented in [21]. The parameters and optimal dimensions of a single cluster of 4 × 4 S-shaped MTS elements were optimized by a parametric study under several key antenna variables (i.e., the substrate dimension, thickness of the upper substrate, length of the rectangular-shaped slot, width of the rectangular-shaped slot, the length of S-shaped MTS element, and the length of S-shaped MTS element including voids between two S-shaped MTS elements) to achieve the wide IBW and ARBW, as followed in [21]: $p = 7.4$ mm, $a = 7$ mm, $c_1 = 1.8$ mm, $c_2 = 3.5$ mm, $c_3 = 2.5$ mm, $G = 34$ mm, $h_1 = 1.6$ mm, $h_2 = 1.6$ mm, $h_3 = 0.8$ mm, $W_g = 8$ mm, $L_g = 12.5$ mm, $W_1 = 1.8$ mm, $g_f = 1.1$ mm, $L_1 = 24$ mm, $W_2 = 2$ mm, and $L_2 = 25$ mm.

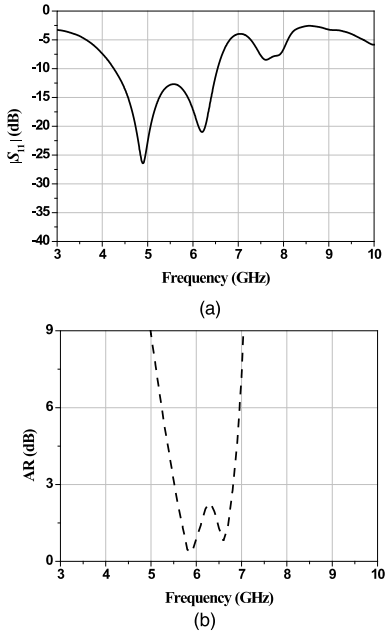

FIGURE 2. Simulated results of a single cluster of 4 × 4 S-shaped MTS elements: (a) IBW, (b) ARBW.

Figures 2(a)-(b) respectively illustrate the simulated IBW and ARBW of one single cluster of 4 × 4 S-shaped MTS elements, given $|S11| \leq -10$ dB and AR ≤ 3 dB. At the center frequency of 5.9 GHz, the simulated IBW of the single cluster of 4 x 4 S-shaped MTS elements was 38.98% (4.2–6.5 GHz), with two resonance frequencies at 4.9 GHz and 6.2 GH. The simulated ARBW was 22% (5.5–6.8 GHz), with two AR troughs of 0.33 dB and 0.8 dB at 5.9 GHz and 6.6 GHz, respectively.

B. SEQUENTIALLY-ROTATED FEED NETWORK

Figure 3(a) shows that the geometry of the proposed sequentially-rotated feed network consisted of seven quarter-wavelength ($\lambda/4$) transformers [22], [23] with different characteristic impedances (Z_i where $i = 1, 2, \ldots, 7$). The geometrical parameters of the proposed sequentially-rotated feed network were shown in Figure 5(d), with corresponding to Table 1. The impedance of the input port (*Port-I*n; Z_0) and four output ports (*Ports 1, 2, 3, 4*; Z_{cp}) were 50 Ω. The output ports were symmetrically aligned and sequentially perpendicular to one another. The sequentially-rotated feed network could achieve phase quadrature with equal magnitude [24].

Figure 3(b) shows the equivalent circuit of the sequentially-rotated feed network [25]. P_0 represents the input power via the feed line, and $P_{in,k}(k = 1, 2, 3, 4)$ represent the power-flow at the output ports. P_{inA}, P_{inB}, and P_{inC} represent the total power-flow between *junctions 1* and *2*, between *junctions 2* and *3*, and subsequent to *junction 3*, respectively. $Z_{in,m}(m = 1, 2, 3, 4)$ represent the impedances at the output ports *(Ports 1, 2, 3, 4)*. Z_{inA}, Z_{inB}, and Z_{inC} represent the impedance between *junctions 1* and *2*, between *junctions 2* and *3*, and subsequent to *junction 3*, respectively.

Based on the equivalent circuit of the sequentially-rotated feed network (Figure 3(b)), the power delivered to each single cluster of 4 × 4 S-shaped MTS elements of the quadri-cluster broadband CP sequentially-rotated MTS-based antenna array can be calculated by (1)–(3) [26].

$$P_{in1} = P_{in2} = P_{in3} = P_{in4} = \frac{1}{4}P_0, \text{ or}$$
$$P_{inC} = P_{in4} = \frac{1}{4}P_0, \tag{1}$$
$$P_{inB} = P_{in3} + P_{inC} = \frac{1}{2}P_0, \tag{2}$$
$$P_{inA} = P_{in2} + P_{inB}. \tag{3}$$

A quarter-wavelength of transmission line [27] was used to determine the characteristic impedances of the sequentially-rotated feed network, following (4)–(10), respectively [28].

$$Z_{in4} = \frac{Z_7^2}{Z_{cp}},\ Z_{inC} = \frac{Z_5^2}{Z_{in3}},\ Z_{in3} = \frac{Z_6^2}{Z_{cp}}, \tag{4}$$
$$Z_{inC} = Z_{in3}, \tag{5}$$

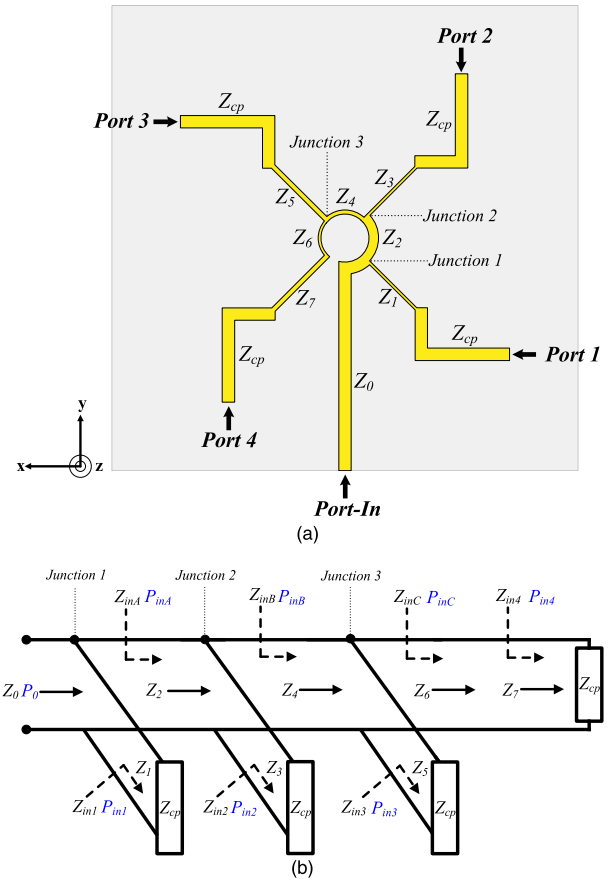

FIGURE 3. The proposed sequentially-rotated feed network: (a) geometry, (b) equivalent circuit.

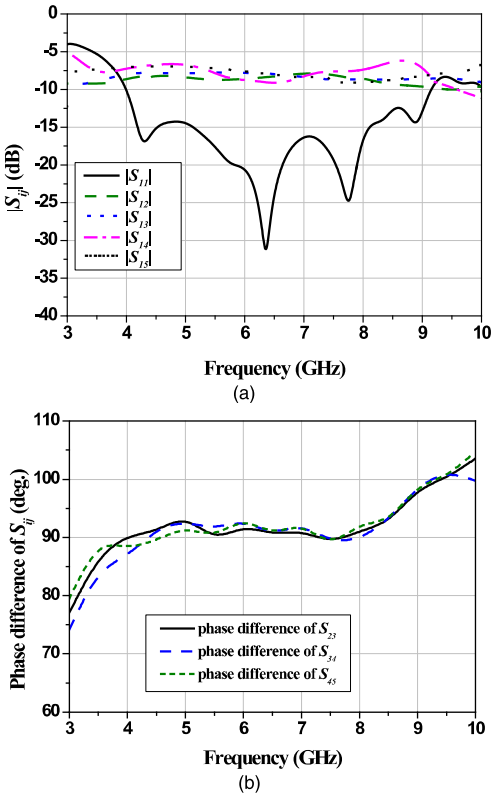

FIGURE 4. Simulated results of the sequentially-rotated feed network: (a) $|S_{ij}|$, (b) phase difference of S_{ij}.

$$Z_{inB} = \frac{Z_4^2}{Z_{in5}||Z_{in6}} = \frac{Z_4^2}{\frac{1}{2}Z_{in3}},\ Z_{inB} = \frac{1}{2}Z_{in2}, \tag{6}$$

$$Z_{in2} = \frac{Z_3^2}{Z_{cp}}, \tag{7}$$

$$Z_{inA} = \frac{Z_2^2}{Z_{in2}||Z_{inB}} = \frac{Z_2^2}{\frac{1}{3}Z_{in2}}, \tag{8}$$

$$Z_{in1} = 3Z_{inA},\ Z_{in1} = \frac{Z_1^2}{Z_{cp}}, \tag{9}$$

$$Z_0 = Z_{in1}||Z_{inA} = \frac{1}{4}Z_{in1}. \tag{10}$$

The sequentially-rotated feed network was optimized by Advanced Design System (ADS) simulation software at the center frequency of 5.9 GHz. The optimal characteristic impedances were as follows: $Z_1 = 100\ \Omega$, $Z_2 = 80\ \Omega$, $Z_3 = 120\ \Omega$, $Z_4 = 62\ \Omega$, $Z_5 = 120\ \Omega$, $Z_6 = 52\ \Omega$, and $Z_7 = 52\ \Omega$.

Figures 4(a)-(b) show the magnitude $|S_{11}|$ of the input port (Port-*In*) and the $|S_{12}|$, $|S_{13}|$, $|S_{14}|$, and $|S_{15}|$ of the output ports (Ports *1,2,3,4*), respectively and the phase difference of *S*-parameters between output ports. In Figure 4(a), the $|S_{11}|$ of the input port was far below -10 dB over 4–9.2 GHz, while those of the output ports were between -5 dB and -10 dB over 4–9 GHz. In Figure 4(b), the phase differences between output ports were approximately 90° over the frequency range of 4–8 GHz.

C. QUADRI-CLUSTER BROADBAND CP SEQUENTIALLY-ROTATED MTS-BASED ANTENNA ARRAY

Figure 5 illustrates the geometry of the quadri-cluster broadband CP sequentially-rotated MTS-based antenna array. The proposed quadri-cluster broadband CP sequentially-rotated MTS-based antenna array was realized by using three layers of FR-4 substrates without air gap between substrates. The upper (h_{S1}), middle (h_{S2}), and lower (h_{S3}) substrates were 1.6 mm, 1.6 mm, and 0.8 mm in thickness. The overall dimension of the substrate was 68 mm × 68 mm ($W_{sub} \times L_{sub}$).

The proposed quadri-cluster broadband CP sequentially-rotated MTS-based antenna array consisted of four clusters of 4 × 4 S-shaped MTS elements: Clusters I, II, III, and IV. The arrangement of the clusters corresponded to the sequentially-rotated feed network. Table 1 tabulates the parameters and optimal dimensions of the quadri-cluster broadband CP sequentially-rotated MTS-based antenna array.

The sense of rotation can be determined by observing the direction of the rotation of the electric field vector as the wave is viewed along the direction of wave propagation. Figure 6 shows the 0°, 90°, 180°, and 270°-phase surface current distribution on partial sections of the quadri-cluster

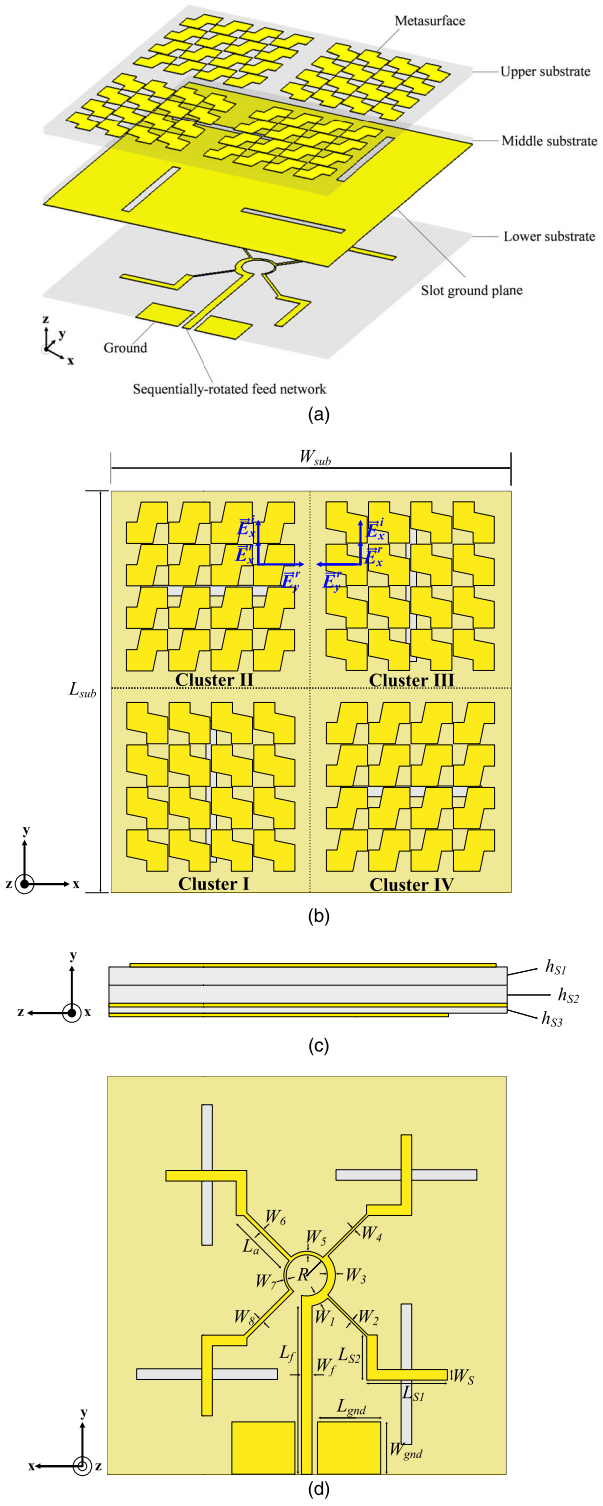

FIGURE 5. Geometry of the quadri-cluster broadband CP sequentially-rotated MTS-based antenna array: (a) schematic view, (b) front view, (c) side view, (d) rear view (reverse side).

broadband CP sequentially-rotated MTS-based antenna array at 5.9 GHz (the center frequency). The electric field vectors moved in the +z direction, resulting in the left-hand circular polarization (LHCP) with counterclockwise rotation.

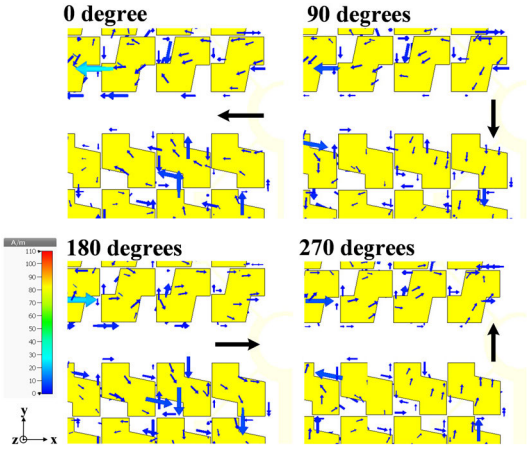

FIGURE 6. Surface current distribution of the quadri-cluster broadband CP sequentially-rotated MTS-based antenna array at 5.9 GHz.

III. RADAR CROSS-SECTION CHARACTERISTICS

Radar cross-section (RCS) is the metric of the reflective or detectable object (target) by radar [29]. The RCS was used in military aircraft, missiles, unmanned aerial vehicles (UAVs), ships, and other military vehicles. For example, a stealth aircraft [30] was designed with a low detectability, so a low RCS characteristic [15] was required for radar detectors. The RCS reduction techniques of the antenna arrays were presented in [31], [32] to achieve a low RCS.

Four clusters of 4 × 4 S-shaped MTS elements on the upper substrate of the proposed quadri-cluster broadband CP sequentially-rotated MTS-based antenna array functioned as the chessboard polarization conversion metasurface (CPCM) [33]. The CPCM was utilized to realize a low RCS by phase cancellation [34] of the reflected wave between adjacent MTS clusters (Figure 5(b)). The co- and cross-polarizations of the reflected wave of the S-shaped MTS element were used to characterize the polarization conversion of the RCS. The co- and cross-polarization can be determined from (11)–(12) [35], respectively

$$R_{xx} = |E_x^r / E_x^i|, \ (co - polarization), \tag{11}$$
$$R_{yx} = |E_y^r / E_x^i|, \ (cross - polarization), \tag{12}$$

where E_x^i is the incident wave of the linearly polarized electric field in the x-direction and E_x^r, E_y^r are the reflected wave of the linearly polarized electric field in the x- and y-directions, respectively. The polarization conversion ratio (PCR) of the PCS is the ratio of polarization conversion characteristic of the S-shaped MTS element. The PCR can be calculated by (13) as [36]

$$PCR = \frac{R_{yx}^2}{R_{yx}^2 + R_{xx}^2}. \tag{13}$$

Figure 7 shows the reflection coefficient (co- and cross-polarizations) and PCR of the S-shaped MTS element. The cross-polarization ($|R_{yx}| \geq -5$ dB) was the major

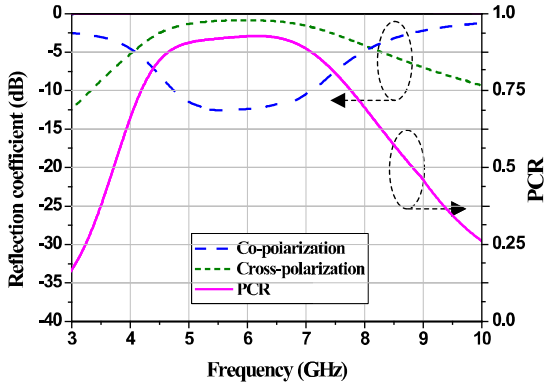

FIGURE 7. Simulated results the reflection coefficient and PCR.

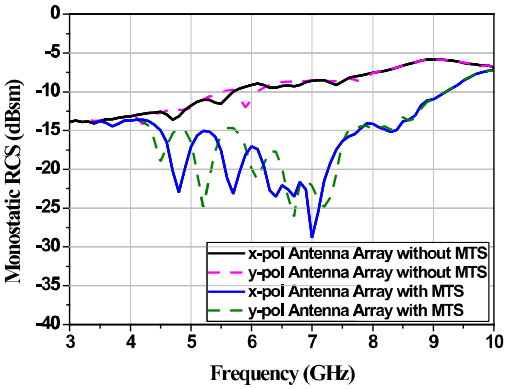

FIGURE 9. Simulated results monostatic RCS.

RCS component between 4–8.1 GHz, while co-polarization ($|R_{xx}| \leq -5$ dB) was failed between 4.1–7.9 GHz. The PCR was over 0.7 with occurred orthogonal electric field at the frequency range of 4.1 −8 GHz, the S-shaped MTS element is suitable for the polarization conversion.

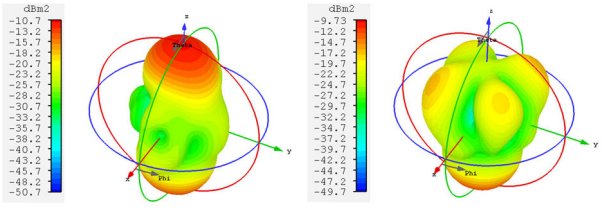

FIGURE 8. 3D bistatic scattered fields at 5.3 GHz under normal incidence wave: (a) the antenna array without four clusters of 4 × 4 S-shaped MTS elements, (b) the proposed quadri-cluster broadband CP sequentially-rotated MTS-based antenna array.

Figures 8(a)-(b) show the 3D bistatic scattered fields at 5.3 GHz under normal incidence wave of the antenna array without four clusters of 4 × 4 S-shaped MTS elements and the proposed quadri-cluster broadband CP sequentially-rotated MTS-based antenna array, respectively. In Figure 8(a), the scattered energy of the antenna array without four clusters of 4 × 4 S-shaped MTS elements was distributed in main lobe along the +z direction. The scattered energy of the proposed quadri-cluster broadband CP sequentially-rotated MTS-based antenna array was slightly decreased in main lobe, while the energy was increased in the four grating lobes $(\varphi, \theta) = (45°, 52°)$, $(135°, 52°)$, $(225°, 52°)$, and $(315°, 52°)$ along the +z direction, as shown in Figure 8(b).

In Figure 9, the monostatic RCS (x- and y-polarizations) of the antenna array without four clusters of 4 × 4 S-shaped MTS elements was above than −13 dBsm. The monostatic RCS of the proposed quadri-cluster broadband CP sequentially-rotated MTS-based antenna array was far below −13.25 dBsm between 4–8.6 GHz. The minimums of the monostatic RCS were −28.84 dBsm (x-pol) and −26 dBsm (y-pol) at 6.6 and 6.3 GHz, respectively. Specially, four clusters of 4 × 4 S-shaped MTS elements of the proposed quadri-cluster broadband CP sequentially-rotated MTS-based antenna array can be reduced the RCS of the antenna array. In addition, the PCR of the S-shaped MTS element achieved a broadband circular-polarization conversion (Figure 7), which is consistent with the RCS reduction of the antenna array (Figure 9) between 4–8 GHz.

IV. PARAMETRIC STUDY

The parametric study was conducted to determine the effects of key parameters of the sequentially-rotated feed network on the IBW and ARBW of the quadri-cluster broadband CP sequentially-rotated MTS-based antenna array. Specifically, the parametric study was consistent with the characteristic impedance variables of the proposed sequentially-rotated feed network. The key parameters under study included the feed line length (L_f: Z_0), the slanted line length (L_a: Z_1, Z_3, Z_5, Z_7), the width of the ring-shaped section between Clusters I and II (W_3: Z_2), the width of the ring-shaped section between Clusters II and III (W_5: Z_4), the width of the ring-shaped section between Clusters II and III (W_7: Z_6), the width of the slanted line of Cluster I (W_2: Z_1, W_4: Z_3), and the width of the slanted line of Cluster III (W_6: Z_5, W_8: Z_7). (Note: $W_1 = W_f$, $W_2 = W_4$ and $W_6 = W_8$).

A. EFFECT OF FEED LINE LENGTH (L_f)

Figures 10(a)-(b) show the simulated IBW and ARBW under different feed line lengths (L_f): 32, 34, and 36 mm, given $|S_{11}| \leq -10$ dB and AR ≤ 3 dB. As shown in Figure 10(a), the IBW covered 4–8.6 GHz and 4–8.5 GHz for $L_f = 32$ and 34 mm, respectively. For $L_f = 36$ mm, an impedance mismatch ($|S_{11}| > -10$ dB) occurred between 5.8–6.6 GHz. In Figure 10(b), AR was greater than 3 dB between 6.9–7.1 GHz for $L_f = 32$ mm. The ARBW covered 4.3–7.63 GHz and 4.3–6.7 GHz for $L_f = 34$ and 36 mm, respectively. The optimal L_f was 34 mm since the ARBW of $L_f = 34$ mm was wider than that of $L_f = 36$ mm. The relation between L_f and Z_0 was as follows: 32, 34, 36 mm, and 48, 50, 41 Ω, respectively. The optimal L_f was 34 mm, which is consistent with the input impedance Z_0 of 50 Ω, since the ARBW of $L_f = 34$ mm was wider than that of $L_f = 36$ mm.

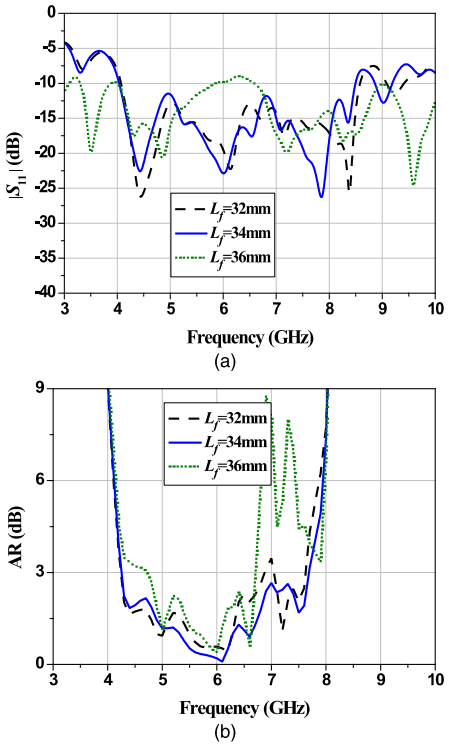

FIGURE 10. Simulated results of the quadri-cluster broadband CP sequentially-rotated MTS-based antenna array under variable L_f: (a) IBW, (b) ARBW.

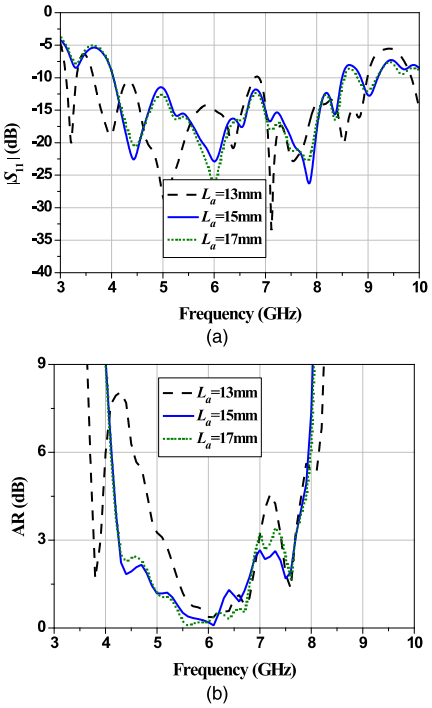

FIGURE 11. Simulated results of the quadri-cluster broadband CP sequentially-rotated MTS-based antenna array under variable L_a: (a) IBW, (b) ARBW.

B. EFFECT OF SLANTED LINE LENGTH (L_a)

Figures 11(a)-(b) show the simulated IBW and ARBW under different slanted line lengths (L_a): 13, 15, and 17 mm, given $|S_{11}| \leq -10$ dB and AR ≤ 3 dB. As shown in Figure 11(a), an impedance mismatch occurred at 6.8 GHz for $L_a = 13$ mm. The IBW were between 4–8.5 GHz for $L_a = 15$ and 17 mm. In Figure 11(b), AR was greater than 3 dB between 3.9–5.2 GHz and 7–7.4 GHz for $L_a = 13$ mm; and at 7 GHz and between 7.2–7.4 GHz for $L_a = 17$ mm. For $L_a = 15$ mm, the ARBW (AR ≤ 3 dB) covered 4.3–7.63 GHz. The relation between L_a and Z_1, Z_3, Z_5, Z_7 shows in Table 2. Specially, as L_a increased, Z_7 was increased. As a result, the optimal L_a was 15 mm, which is consistent with Z_1, Z_3, Z_5, Z_7 of 100, 120, 120, 52 Ω, respectively.

TABLE 2. Relation between L_a and Z_1, Z_3, Z_5, Z_7.

L_a (mm)	Z_1 (Ω)	Z_3 (Ω)	Z_5 (Ω)	Z_7 (Ω)
13	83	97	82	34
15	100	120	120	52
17	97	116	114	71

C. EFFECT OF WIDTH OF RING-SHAPED SECTION BETWEEN CLUSTERS I AND II (W_3)

Figures 12(a)-(b) illustrate the simulated IBW and ARBW under variable widths of the ring-shaped section between Clusters I and II (W_3): 1.2, 1.4, and 1.6 mm. As W_3 increased from 1.2 to 1.6 mm, $|S_{11}|$ of the first and third resonances deteriorated (from −28.5 dB to −18 dB and −39 dB to −23 dB, respectively), while that of the second resonance improved. The AR was larger than 3 dB at 7 and 7.4 GHz for $W_3 = 1.2$ and 1.6 mm, respectively. The ARBW (AR ≤ 3 dB) covered 4.3–7.63 GHz for $W_3 = 1.4$ mm. The relation between W_3 and Z_2 was as follows: 1.2, 1.4, 1.6 mm, and 97, 80, 68 Ω, respectively. As W_3 increased, Z_2 was decreased. As a result, the optimal W_3 was 1.4 mm, which is consistent with Z_2 of 80 Ω.

D. EFFECT OF WIDTH OF RING-SHAPED SECTION BETWEEN CLUSTERS II AND III (W_5)

Figures 13(a)-(b) illustrate the simulated IBW and ARBW under variable widths of the ring-shaped section between Clusters II and III (W_5): 0.4, 0.6, and 0.8 mm. As W_5 increased from 0.4 to 0.8 mm, $|S_{11}|$ of the first and third resonances improved (from −20 dB to −26 dB and −22.5 dB to −32.5 dB, respectively), while that of the second resonance deteriorated. The AR was larger than 3 dB between 7.3–7.4 GHz and 6.9–7.2 GHz for $W_5 = 0.4$ and 0.8 mm, respectively. The relation between W_5 and Z_4 was as follows: 0.4, 0.6, 0.8 mm, and 68, 62, 59 Ω, respectively. As W_5 increased, Z_4 was decreased. For $W_5 = 0.6$ mm, the ARBW (AR ≤ 3 dB) was between 4.3–7.63 GHz, which is consistent with Z_4 of 62 Ω.

E. EFFECT OF WIDTH OF RING-SHAPED SECTION BETWEEN CLUSTERS III AND IV (W_7)

Figures 14(a)-(b) illustrate the simulated IBW and ARBW under variable widths of the ring-shaped section between Clusters III and IV (W_7): 0.2, 0.4, and 0.6 mm. As W_7

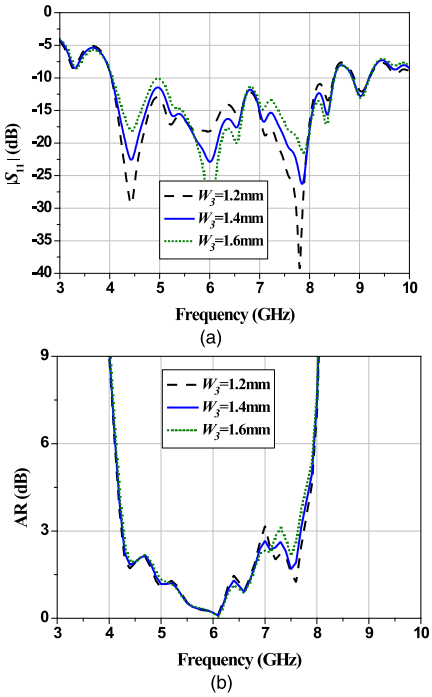

FIGURE 12. Simulated results of the quadri-cluster broadband CP sequentially-rotated MTS-based antenna array under variable W_3: (a) IBW, (b) ARBW.

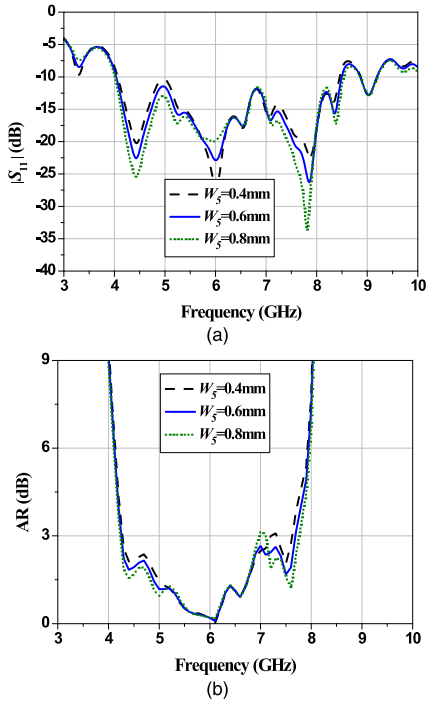

FIGURE 13. Simulated results of the quadri-cluster broadband CP sequentially-rotated MTS-based antenna array under variable W_5: (a) IBW, (b) ARBW.

increased from 0.2 to 0.6 mm, $|S_{11}|$ of the first and third resonance deteriorated (from −24 dB to −22 dB and −34 dB to −22.5 dB, respectively), while that of the second resonance improved. The AR was larger than 3 dB at 7 GHz and 7.2–7.4 GHz for W_7 = 0.2 and 0.6 mm, respectively. The widest ARBW (4.3–7.63 GHz) was achieved with

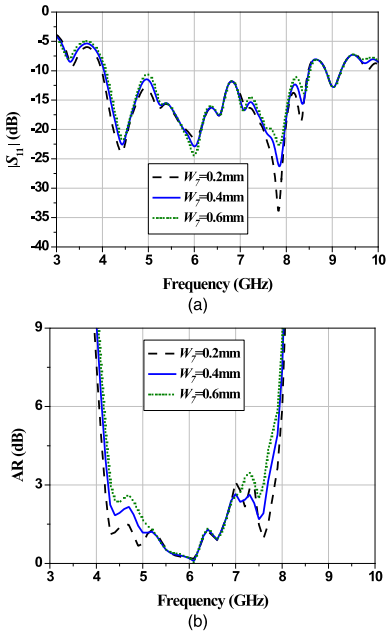

FIGURE 14. Simulated results of the quadri-cluster broadband CP sequentially-rotated MTS-based antenna array under variable W_7: (a) IBW, (b) ARBW.

W_7 = 0.4 mm. The relation between W_7 and Z_6 was as follows: 0.2, 0.4, 0.6 mm, and 56, 52, 43 Ω, respectively. As W_7 increased, Z_6 was decreased. As a result, the optimal W_7 was 0.4 mm, which is consistent with Z_6 of 52 Ω.

F. EFFECT OF WIDTH OF SLANTED LINE OF CLUSTER I (W_2)

Figures 15(a)-(b) illustrate the simulated IBW and ARBW under variable widths of the slanted line of Cluster I (W_2): 0.2, 0.4, and 0.6 mm. As W_2 increased from 0.2 to 0.6 mm, $|S_{11}|$ of the first and third resonances deteriorated (from −30.5 dB to −19 dB and −29 dB to −25 dB, respectively), while that of the second resonance improved. The ARBW (AR ≤ 3 dB) were between 4.2–7.3 GHz and 4.2–7.63 GHz for W_3 = 0.2 and 0.4 mm, respectively. Meanwhile, the AR was larger than 3 dB at 7 GHz for W_2 = 0.6 mm. The ARBW of W_3 = 0.4 mm was slightly wider than that of W_3 = 0.2, so W_3 = 0.4 mm was selected, which is consistent with Z_1, Z_3 of 100, 120 Ω, respectively. The relation between $W_2 = W_4$ and Z_1, Z_3 shows in Table 3. As $W_2 = W_4$ increased, both Z_1 and Z_3 were increased.

TABLE 3. Relation between $W_2 = W_4$ and Z_1, Z_3.

$W_2 = W_4$ (mm)	Z_1 (Ω)	Z_3 (Ω)
0.2	97	118
0.4	100	120
0.6	105	123

G. EFFECT OF WIDTH OF SLANTED LINE OF CLUSTER III (W_6)

Figures 16(a)-(b) illustrate the simulated IBW and ARBW under variable widths of the slanted line of Cluster III

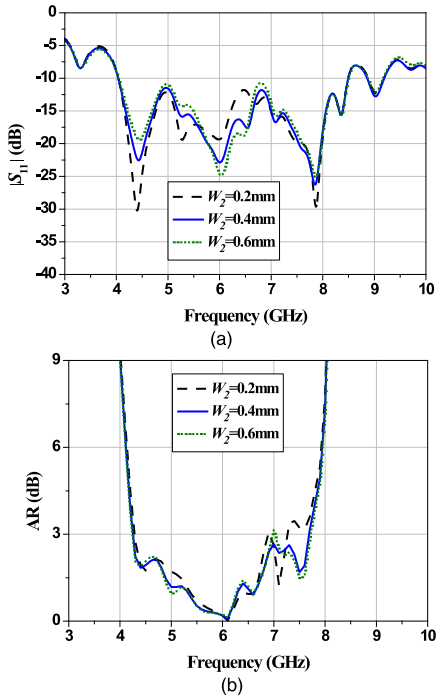

FIGURE 15. Simulated results of the quadri-cluster broadband CP sequentially-rotated MTS-based antenna array under variable W_2: (a) IBW, (b) ARBW.

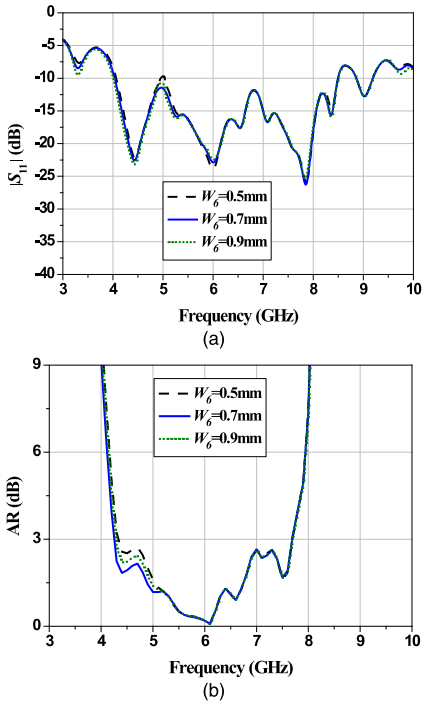

FIGURE 16. Simulated results of the quadri-cluster broadband CP sequentially-rotated MTS-based antenna array under variable W_6: (a) IBW, (b) ARBW.

TABLE 4. Relation between $W_6 = W_8$ and Z_5, Z_7.

$W_6 = W_8$ (mm)	Z_5 (Ω)	Z_7 (Ω)
0.5	115	49
0.7	120	52
0.9	122	55

(W_6): 0.5, 0.7, and 0.9 mm. An impedance mismatch occurred at 5 GHz for $W_6 = 0.5$ mm, while $|S_{11}|$ was between 4–8.5 GHz for $W_6 = 0.7$ and 0.9 mm. The variation in W_6 had a minimal effect on the ARBW of the quadri-cluster broadband CP sequentially-rotated MTS-based antenna array, as shown in Figure 16(b). The relation between $W_6 = W_8$ and Z_5, Z_7 shows in Table 4. As $W_6 = W_8$ increased, both Z_5 and Z_7 were increased. The optimal $W_6 = W_8$ was 0.7 mm, which is consistent with Z_5, Z_7 of 120, 52 Ω, respectively.

V. EXPERIMENTAL RESULTS

To validate the simulation results, a prototype antenna was fabricated by the PCB fabrication technology and experiments were carried out. Figure 17 depicts the front and rear of the quadri-cluster broadband CP sequentially-rotated MTS-based antenna array prototype for C-band satellite communications. In the antenna fabrication, the left and right sides of the substrates of the prototype antenna were 3 mm wider than the antenna schematic (Figure 5) so as to mount the three substrate layers together.

Figure 18 shows the measurement setup in an anechoic chamber, where the prototype antenna was used as the receiving antenna and the standard CP spiral antennas (ETS-Lindgren Model 3102 Series Conical Log Spiral antennas [37]) was used as the transmitting antenna. A pair of ETS-Lindgren Model 3102 Series Conical Log Spiral antennas was used to verify the LHCP and RHCP radiations of the prototype antenna, as shown in Figure 19.

The far-field region is the distance requirement between the transmitting antenna and receiving antenna. The distance was more than R meters that can be determined by (14)

$$R \geq \frac{2D^2}{\lambda} \tag{14}$$

where R is the distance between the transmitting antenna and receiving antenna, D is the largest dimension of the antenna under test, and λ is the shortest wavelength along the operating frequency. In this case, the distance of 4 meters was used.

The experiments were measured by using a vector network analyzer (ZVB 20 model). The measurement procedure consisted of two steps. The first step was to calibrate the vector network analyzer using a calibration kit (ZV-Z235). The second step was the measurement. The antenna performance metrics included the magnitude of reflection coefficient ($|S_{11}|$), AR, radiation pattern, and gain.

The AR was carried out by measurement of the electric field from LHCP and RHCP radiations of the transmitting antenna. The co-polarization (co-pol) and cross-polarization (x-pol) of the electric field between the transmitting and receiving antennas were corresponding to the same sense ($|E_{co-pol}|$) and opposite sense (E_{x-pol}), respectively. The prototype antenna radiates LHCP (Figure 6). The co-polarization and cross-polarization are consistent with LHCP and RHCP radiations, respectively. The AR can be determined from

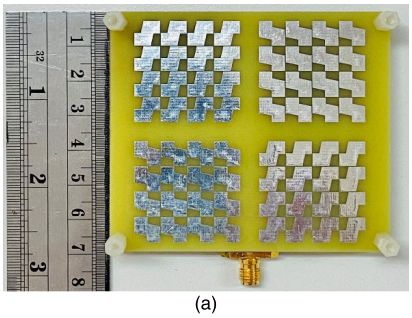
(a)

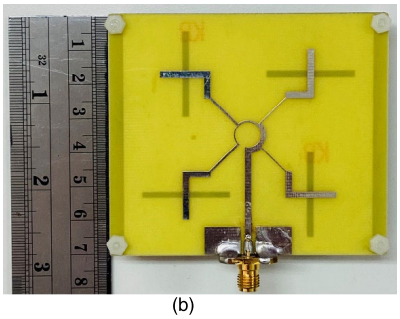
(b)

FIGURE 17. Prototype of the quadri-cluster broadband CP sequentially-rotated MTS-based antenna array: (a) front view, (b) rear view.

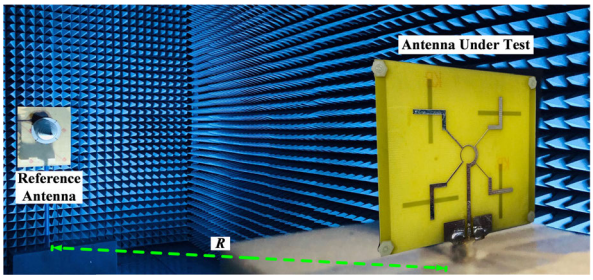

FIGURE 18. Measurement setup in an anechoic chamber.

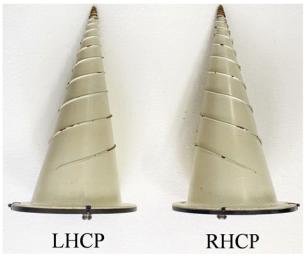

FIGURE 19. ETS-lindgren model 3102 series conical log spiral antennas.

equation (15) as [38]

$$AR(dB) = 20log\left(\frac{|E_{co-pol}| + |E_{x-pol}|}{|E_{co-pol}| - |E_{x-pol}|}\right), \qquad (15)$$

where $|E_{co-pol}|$ and $|E_{x-pol}|$ are the electric field magnitude of the co-polarization and cross-polarization respectively, between the transmitting and receiving antennas.

Figures 20(a)-(b) compare the simulated and measured IBW and ARBW of the quadri-cluster broadband CP sequentially-rotated MTS-based antenna array at 5.9 GHz (the center frequency), given $|S_{11}| \leq -10$ dB and AR ≤ 3 dB.

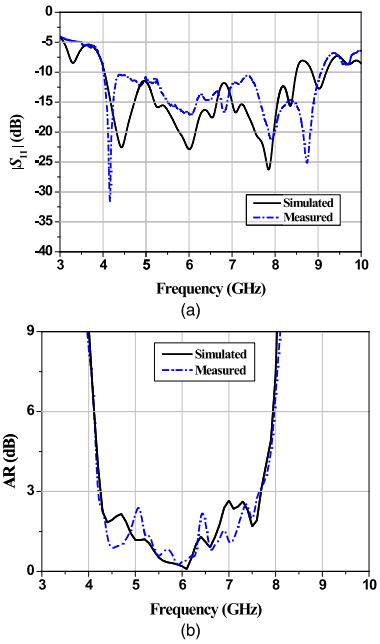

FIGURE 20. Simulated and measured results of the quadri-cluster broadband CP sequentially-rotated MTS-based antenna array: (a) IBW, (b) ARBW.

The simulated IBW and ARBW were 74.57% (4–8.4 GHz) and 56.4% (4.3–7.63 GHz, respectively), and the measured IBW and ARBW were 87.74% (4–9 GHz) and 57.6% (4.2–7.6 GHz, respectively). The simulated and measured results were agreeable.

Figures 21(a)-(c) show the simulated and measured LHCP and right-hand circular polarization (RHCP) radiation patterns of the quadri-cluster broadband CP sequentially-rotated MTS-based antenna array in the xz- and yz-planes at 4.3, 5.9, and 7.6 GHz, respectively. The simulated and measured LHCP were in good agreement, while those of RHCP were satisfactorily agreeable. Since the upper measured ARBW (AR $\leq$ 3 dB) of the quadri-cluster broadband CP sequentially-rotated MTS-based antenna array was at 7.63 GHz (Figure 20(b)), the LHCP and RHCP radiation patterns were thus simulated and measured at 7.6 GHz (Figure 16(c)).

Figures 22(a)-(b) compare the simulated and measured boresight gain bandwidth and radiation efficiency of the quadri-cluster broadband CP sequentially-rotated MTS-based antenna array. The simulated and measured 3-dB boresight gain bandwidths were 55.9% (3.9–7.2 GHz) and 81.3% (3.9–8.7 GHz), respectively. The relatively large differences between the simulated and measured 3-dB boresight gain bandwidth and radiation efficiency were attributable to the wider measured IBW (4–9 GHz), vis-à-vis the simulated IBW (4–8.4 GHz), as shown in Figure 20(a). Also, the measured radiation efficiency beyond 8 GHz was improved with the same reason. The simulated and measured maximum gains were 10.34 dBic at 5.7 GHz and 10.04 dBic at 5.6 GHz, respectively.

Overall, the measured radiation efficiency over the C-band frequency spectrum (4–8 GHz) was more than 60%.

TABLE 5. Comparison between existing CP MTS-based antenna arrays and the quadri-cluster broadband CP sequentially-rotated MTS-based antenna array.

References	f_0 (GHz)	-10-dB IBW (%)	3-dB ARBW (%)	3-dB boresight gain BW (%)	Maximum gain (dBic)	Electrical dimension
[19]	6.4	32.60	26.35	Not given	13.50	$2.06\,\lambda_0 \times 2.06\,\lambda_0 \times 0.080\,\lambda_0$
[20]	5.9	58.06	41.67	37.30	12.08	$1.26\,\lambda_0 \times 1.26\,\lambda_0 \times 0.046\,\lambda_0$
[33]	9.0	13.80	21.11	Not given	11.20	$1.81\,\lambda_0 \times 1.81\,\lambda_0 \times 4.280\,\lambda_0$
[36]	5.2	34.60	34.60	23.90	12.15	$1.34\,\lambda_0 \times 1.34\,\lambda_0 \times 0.006\,\lambda_0$
[39]	5.0	38.60	32.00	Not given	11.18	$1.40\,\lambda_0 \times 1.40\,\lambda_0 \times 0.069\,\lambda_0$
[40]	9.6	54.68	40.00	30.70	12.20	$1.45\,\lambda_0 \times 1.45\,\lambda_0 \times 0.072\,\lambda_0$
This work	**5.9**	**84.74**	**57.60**	**81.30**	**10.04**	$\mathbf{0.90\,\lambda_0 \times 0.90\,\lambda_0 \times 0.053\,\lambda_0}$

λ_0: the free-space wavelength at the lowest operating frequency of the CP MTS-based antenna arrays
f_0: the center frequency of the CP MTS-based antenna arrays

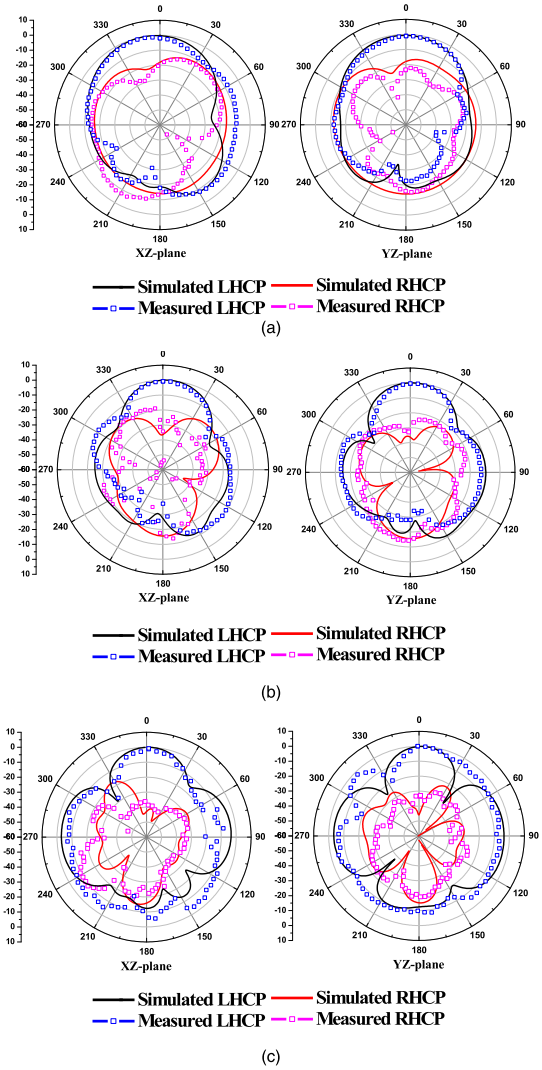

FIGURE 21. Simulated and measured LHCP (co-polarized) and RHCP (cross-polarized) radiation patterns at: (a) 4.3 GHz, (b) 5.9 GHz, (c) 7.6 GHz.

In addition, the quadri-cluster broadband CP sequentially-rotated MTS-based antenna array could achieve IBW and ARBW of 87.74% (4–9 GHz) and 57.6% (4.2–7.6 GHz),

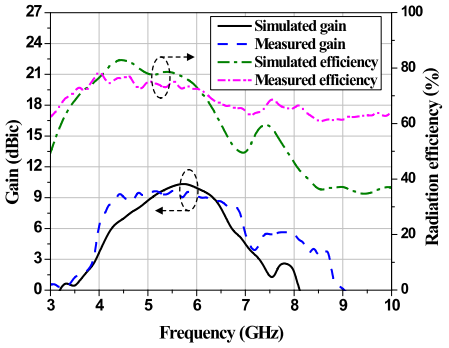

FIGURE 22. Simulated and measured boresight gain bandwidth and radiation efficiency of the quadri-cluster broadband CP sequentially-rotated MTS-based antenna array.

respectively. The wide IBW and ARBW thus render the quadri-cluster sequentially-rotated MTS-based antenna scheme suitable for satellite communication applications.

Table 5 compares the existing CP MTS-based antenna arrays with the proposed quadri-cluster broadband CP sequentially-rotated MTS-based antenna array with respect to IBW, 3-dB ARBW, 3-dB boresight gain bandwidth, maximum gain, and electrical dimension. In [19], the 2 × 2 MTS-based antenna array with sequentially-rotated feed network achieved high gain but suffered from narrow IBW and ARBW. Besides, the antenna design was very complex since through-holes had to be drilled between MTS and the ground plane substrate.

In [20], the MTS-based antenna array using sequentially-rotated series-parallel feed network achieved wide IBW and ARBW but suffered from bulkiness. In [33], the 2 × 2 multi-layered MTS slot antenna array achieved high gain but narrow IBW and ARBW. The antenna was very bulky due to the large air gap between the MTS substrate and the slot antenna substrate. In [36], the 2 × 2 MTS-based slot antenna array using sequentially-rotated feed network achieved high gain but narrow IBW and ARBW, apart from bulkiness.

In [39], the dual-feeding MTS-based antenna array suffered from bulkiness and the IBW and ARBW were narrow. In addition, the antenna feed network design was complex.

In [40], the antenna achieved wide IBW and ARBW but suffered from bulkiness.

In addition, the quadri-cluster of S-shaped MTS elements performed as circularly polarized (CP) antenna arrays. In order to achieve a perfectly circular polarization, it required four-ports of the feed network to provide the phase quadrature with equal magnitude. The sequentially-rotated feed network was proposed to serve that requirement. Also, the sequentially-rotated feed network was fed by a single-fed of the coplanar waveguide functioning as an input port. The quadri-cluster of S-shaped MTS elements CP antenna arrays with sequentially-rotated feed network can enhance the performance of the single-cluster of S-shaped MTS elements, in terms of the IBW (84.74%, 4–9 GHz), 3-dB ARBW (57.6%, 4.2–7.6 GHz), as well as 3-dB boresight gain bandwidth (81.3%, 3.9–8.7 GHz). The wideband and low RCS of the proposed quadri-cluster broadband CP sequentially-rotated MTS-based antenna array was far below −13.25 dBsm, consistent with the CP conversion at the operating frequency. The wide IBW, ARBW, and low RCS thus render the quadri-cluster sequentially-rotated MTS-based antenna scheme suitable for satellite communication applications.

VI. CONCLUSION

This research proposed a compact quadri-cluster broadband CP sequentially-rotated MTS-based antenna array for C-band satellite communications. One cluster of the quadri-cluster antenna array consisted of 4×4 periodically-arranged S-shaped MTS elements. In the study, simulations were first carried out for the optimal parameter dimensions, and an antenna prototype was fabricated and experiments were undertaken. The simulated IBW and ARBW at the center frequency (5.9 GHz) were 74.57% (4–8.4 GHz) and 56.4% (4.3–7.63 GHz), given $|S_{11}| \leq -10$ dB and AR ≤ 3 dB, with the 3-dB boresight gain bandwidth of 55.9% (3.9–7.2 GHz), and low radar cross-section. The measured IBW, ARBW, and 3-dB boresight gain bandwidth were 87.74% (4–9 GHz), 57.6% (4.2–7.6 GHz), and 81.3% (3.9–8.7 GHz), respectively. Besides, the measured maximum gain and radiation efficiency were 10.04 dBic at 5.6 GHz and over 60% in the C-band frequency spectrum. The results also showed that the simulated and measured LHCP radiation patterns were in good agreement. Essentially, the wide IBW and ARBW of the quadri-cluster broadband CP sequentially-rotated MTS-based antenna array of 87.74% (4–9 GHz) and 57.6% (4.2–7.6 GHz) render the proposed antenna scheme operationally suitable for satellite communications into CP wave by the S-shaped MTS elements.

REFERENCES

[1] N. Hussain, M.-J. Jeong, A. Abbas, T.-J. Kim, and N. Kim, "A metasurface-based low-profile wideband circularly polarized patch antenna for 5G millimeter-wave systems," *IEEE Access*, vol. 8, pp. 22127–22135, 2020.

[2] Y. Juan, W. Yang, and W. Che, "Miniaturized low-profile circularly polarized metasurface antenna using capacitive loading," *IEEE Trans. Antennas Propag.*, vol. 67, no. 5, pp. 3527–3532, May 2019.

[3] L. Garcia-Gamez, L. Bernard, S. Collardey, H. Covic, R. Sauleau, K. Mahdjoubi, P. Potier, and P. Pouliguen, "Compact GNSS metasurface-inspired cavity antennas," *IEEE Antennas Wireless Propag. Lett.*, vol. 18, no. 12, pp. 2652–2656, Dec. 2019.

[4] Z. Wu, L. Li, Y. Li, and X. Chen, "Metasurface superstrate antenna with wideband circular polarization for satellite communication application," *IEEE Antennas Wireless Propag. Lett.*, vol. 15, pp. 374–377, 2016.

[5] X.-Z. Lai, Z.-M. Xie, Q.-Q. Xie, and X.-L. Cen, "A dual circularly polarized RFID reader antenna with wideband isolation," *IEEE Antennas Wireless Propag. Lett.*, vol. 12, pp. 1630–1633, 2013.

[6] G. Xiao, P. Aflaki, S. Lang, Z. Zhang, Y. Tao, C. Py, P. Lu, C. Martin, and S. Change, "Printed UHF RFID reader antennas for potential retail applications," *IEEE J. Radio Freq. Identificat.*, vol. 2, no. 1, pp. 31–37, Mar. 2018.

[7] J. Lu, H. C. Zhang, C. Wei, J.-S. Hong, and T. J. Cui, "Design of compact circularly polarized antenna using sunshine-shaped slotted patch," *IEEE Trans. Antennas Propag.*, vol. 68, no. 9, pp. 6800–6805, Sep. 2020.

[8] N. Rasool, H. Kama, M. Abdul Basit, and M. Abdullah, "A low profile high gain ultra lightweight circularly polarized annular ring slot antenna for airborne and airship applications," *IEEE Access*, vol. 7, pp. 155048–155056, 2019.

[9] S. Liu, D. Yang, and J. Pan, "A low-profile broadband dual-circularly-polarized metasurface antenna," *IEEE Antennas Wireless Propag. Lett.*, vol. 18, no. 7, pp. 1395–1399, Jul. 2019.

[10] S. Liu, D. Yang, and J. Pan, "A low-profile circularly polarized metasurface antenna with wide axial-ratio beamwidth," *IEEE Antennas Wireless Propag. Lett.*, vol. 18, no. 7, pp. 1438–1442, Jul. 2019.

[11] S. X. Ta and I. Park, "Low-profile broadband circularly polarized patch antenna using metasurface," *IEEE Trans. Antennas Propag.*, vol. 63, no. 12, pp. 5929–5934, Dec. 2015.

[12] S. X. Ta, J. J. Lee, and I. Park, "Solar-cell metasurface-integrated circularly polarized antenna with 100% insolation," *IEEE Antennas Wireless Propag. Lett.*, vol. 16, pp. 2675–2678, 2017.

[13] H. L. Zhu, S. W. Cheung, X. H. Liu, and T. I. Yuk, "Design of polarization reconfigurable antenna using metasurface," *IEEE Trans. Antennas Propag.*, vol. 62, no. 6, pp. 2891–2898, Jun. 2014.

[14] C. Ni, M. S. Chen, Z. X. Zhang, and X. L. Wu, "Design of frequency- and polarization-reconfigurable antenna based on the polarization conversion metasurface," *IEEE Antennas Wireless Propag. Lett.*, vol. 17, no. 1, pp. 78–81, Jan. 2018.

[15] Y. Jia, Y. Liu, S. Gong, W. Zhang, and G. Liao, "A low-RCS and high-gain circularly polarized antenna with a low profile," *IEEE Antennas Wireless Propag. Lett.*, vol. 16, pp. 2477–2480, 2017.

[16] Y. Fan, J. Wang, Y. Li, J. Zhang, Y. Han, and S. Qu, "Low-RCS and high-gain circularly polarized metasurface antenna," *IEEE Trans. Antennas Propag.*, vol. 67, no. 12, pp. 7197–7203, Dec. 2019.

[17] C. Li, X.-W. Zhu, P. Liu, C. Yu, and W. Hong, "A metasurface-based multilayer wideband circularly polarized patch antenna array with a parallel feeding network for Q-band," *IEEE Antennas Wireless Propag. Lett.*, vol. 18, no. 6, pp. 1208–1212, Jun. 2019.

[18] S. Karamzadeh and V. Rafiei, "Modification of metasurface-based CP array antenna by using cascade feed network," *IET Microw., Antennas Propag.*, vol. 13, no. 9, pp. 1334–1337, Jul. 2019.

[19] W. Zhang, Y. Liu, and Y. Jia, "Circularly polarized antenna array with low RCS using metasurface-inspired antenna units," *IEEE Antennas Wireless Propag. Lett.*, vol. 18, no. 7, pp. 1453–1457, Jul. 2019.

[20] S. X. Ta and I. Park, "Compact wideband circularly polarized patch antenna array using metasurface," *IEEE Antennas Wireless Propag. Lett.*, vol. 16, pp. 1932–1936, 2017.

[21] N. Supreeyatitikul, T. Lertwiriyaprapa, and C. Phongcharoenpanich, "S-shaped metasurface-based wideband circularly polarized patch antenna for C-Band applications," *IEEE Access*, vol. 9, pp. 23944–23955, 2021.

[22] M. N. Jazi and M. N. Azarmanesh, "Design and implementation of circularly polarised microstrip antenna array using a new serial feed sequentially rotated technique," *IEE Proc. Microw., Antennas Propag.*, vol. 153, no. 2, pp. 133–140, Apr. 2006.

[23] S. Mohammadi-Asl, J. Nourinia, C. Ghobadi, and M. Majidzadeh, "Wideband compact circularly polarized sequentially rotated array antenna with sequential-phase feed network," *IEEE Antennas Wireless Propag. Lett.*, vol. 16, pp. 3176–3179, 2017.

[24] S.-K. Lin and Y.-C. Lin, "A compact sequential-phase feed using uniform transmission lines for circularly polarized sequential-rotation arrays," *IEEE Trans. Antennas Propag.*, vol. 59, no. 7, pp. 2721–2724, Jul. 2011.

[25] D. Inserra, G. Wen, and W. Hu, "Sequentially rotated circular antenna array with curved PIFA and series feed network," *IEEE Trans. Antennas Propag.*, vol. 66, no. 11, pp. 5849–5858, Nov. 2018.
[26] S. Gao, Y. Qin, and A. Sambell, "Low-cost broadband circularly polarized printed antennas and array," *IEEE Antennas Propag. Mag.*, vol. 49, no. 4, pp. 57–64, Aug. 2007.
[27] C. A. Balanis, *Antenna Theory: Analysis and Design*, 3rd ed. Hoboken, NJ, USA: Wiley, 2005.
[28] A. Chen, Y. Zhang, Z. Chen, and S. Cao, "A Ka-band high-gain circularly polarized microstrip antenna array," *IEEE Antennas Wireless Propag. Lett.*, vol. 9, pp. 1115–1118, 2010.
[29] C. M. Dikmen, S. Çimen, and G. Çakır, "Planar octagonal-shaped UWB antenna with reduced radar cross section," *IEEE Trans. Antennas Propag.*, vol. 62, no. 6, pp. 2946–2953, Jun. 2014.
[30] M. A. Alves, R. J. Port, and M. C. Rezende, "Simulations of the radar cross section of a stealth aircraft," in *IEEE MTT-S Int. Microw. Symp. Dig.*, Salvador, Brazil, 2007, pp. 409–412.
[31] Y. Zhao, X. Cao, J. Gao, X. Yao, and X. Liu, "A low-RCS and high-gain slot antenna using broadband metasurface," *IEEE Antennas Wireless Propag. Lett.*, vol. 15, pp. 290–293, Jun. 2016.
[32] Q. Chen, M. Guo, D. Sang, Z. Sun, and Y. Fu, "RCS reduction of patch array antenna using anisotropic resistive metasurface," *IEEE Antennas Wireless Propag. Lett.*, vol. 18, no. 6, pp. 1223–1227, Jun. 2019.
[33] K. Li, Y. Liu, Y. Jia, and Y. J. Guo, "A circularly polarized high-gain antenna with low RCS over a wideband using chessboard polarization conversion metasurfaces," *IEEE Trans. Antennas Propag.*, vol. 65, no. 8, pp. 4288–4292, Aug. 2017.
[34] Z. Liu, S. Liu, J. Bornemann, X. Zhao, X. Kong, Z. Huang, B. Bian, and D. Wang, "A low-RCS, high-GBP Fabry–Perot antenna with embedded chessboard polarization conversion metasurface," *IEEE Access*, vol. 8, pp. 80183–80194, 2020.
[35] Y. Liu, K. Li, Y. Jia, Y. Hao, S. Gong, and Y. J. Guo, "Wideband RCS reduction of a slot array antenna using polarization conversion metasurfaces," *IEEE Trans. Antennas Propag.*, vol. 64, no. 1, pp. 326–331, Jan. 2016.
[36] Q. Zheng, C. Guo, and J. Ding, "Wideband and low RCS planar circularly polarized array based on polarization conversion of metasurface," *Microw. Opt. Technol. Lett.*, vol. 60, no. 3, pp. 784–789, Mar. 2018.
[37] ETS-Lindgren. (2013). *3102 Conical Log Spiral Antenna*. Accessed: Mar. 8, 2021. [Online]. Available: http://www.ets lindgren.com/products/antennas/conical-log-spiral/4011/401102
[38] A. Sakonkanapong and C. Phongcharoenpanich, "Near-field HF-RFID and CMA-based circularly polarized far-field UHF-RFID integrated tag antenna," *Int. J. Antennas Propag.*, vol. 2020, pp. 1–15, Apr. 2020.
[39] W. Yang, Q. Meng, W. Che, L. Gu, and Q. Xue, "Low-profile wideband dual-circularly polarized metasurface antenna array with large beamwidth," *IEEE Antennas Wireless Propag. Lett.*, vol. 17, no. 9, pp. 1613–1616, Sep. 2018.
[40] L. Zhang, C. Liu, C. Ni, M. Kong, and X. Wu, "Low-RCS, circular polarization, and high-gain broadband antenna based on mirror polarization conversion metasurfaces," *Int. J. Antennas Propag.*, vol. 2019, pp. 1–8, Aug. 2019.

NATHAPAT SUPREEYATITIKUL was born in Nakhon Si Thammarat, Thailand, in 1991. He received the B.Eng. degree from Mahidol University, Thailand, in 2014, and the M.Eng. degree from the King Mongkut's University of Technology Thonburi (KMUTT), Thailand, in 2016. He is currently pursuing the D.Eng. degree with the King Mongkut's Institute of Technology Ladkrabang (KMITL). His research interests include circularly polarized antennas and MIMO antennas.

DANAI TORRUNGRUENG (Senior Member, IEEE) received the B.Eng. degree in electrical engineering from Chulalongkorn University, Bangkok, Thailand, in 1993, and the M.S. and Ph.D. degrees in electrical engineering from The Ohio State University, Columbus, OH, USA, in 1996 and 2000, respectively. From 1995 to 2000, he was a Graduate Research Assistant (GRA) with the ElectroScience Laboratory, Department of Electrical Engineering, The Ohio State University. Prior to joining Asian University in Thailand, in 2002, he worked as a Senior Engineer in the USA, involved in research and development of the urban propagation modeling project. He is currently a Professor with the Department of Teacher Training in Electrical Engineering, Faculty of Technical Education, King Mongkut's University of Technology North Bangkok, Bangkok. In 2000, he won an award in the National URSI Student Paper competition at the 2000 National Radio Science Meeting, Boulder, CO, USA. From 2004 to 2009, he invented generalized Smith charts, called T-charts or Meta-Smith charts, for solving several problems associated with conjugately characteristic-impedance transmission lines (CCITLs) and bi-characteristic-impedance transmission lines (BCITLs), including their useful applications in applied electromagnetics. He has authored *MetaSmith Charts and Their Potential Applications (Synthesis Lectures on Antennas)* (Morgan & Claypool, 2010) and *Advanced Transmission-Line Modeling in Electromagnetics* (CharansanitwongPrinting, 2012). His research interests include electromagnetic sensors, fast computational electromagnetics, rough surface scattering, propagation modeling, electromagnetic wave theory, microwave theory and techniques, and antennas. He is also a member of the ECTI, where he has served as an ECTI Technical Chair for Electromagnetics, from 2014 to 2017. In addition, he has also served as a TPC Co-Chair for TJMW2016, the Vice Co-Chair for TJMW2017, and the TPC Chair for ISAP2017. Furthermore, he is also a Co-Founder of the Innovative Electromagnetics Academy of Thailand (iEMAT) founded in 2013.

CHUWONG PHONGCHAROENPANICH (Member, IEEE) received the B.Eng. (Hons.) degree in telecommunications engineering and the M.Eng. and D.Eng. degrees in electrical engineering from the King Mongkut's Institute of Technology Ladkrabang (KMITL), Bangkok, Thailand, in 1996, 1998, and 2001, respectively. He is currently an Associate Professor with the Department of Telecommunications Engineering, KMITL, where he also serves as the Leader for the Innovative Antenna and Electromagnetic Applications Research Laboratory. His research interests include antenna design for various mobile and wireless communications, array antennas, and electromagnetic theory and applications. He is also a member of IEICE and ECTI. He has served as the Chair of the IEEE MTT/AP/ED Thailand Chapter, from 2014 to 2018. He has been on organizing committee of several international conferences, including the TPC Chair of 2009 International Symposium on Antennas and Propagation (ISAP 2009), a TPC Member of ISAP 2012, and the Vice Chair of ISAP 2017. He is also a Reviewer of many scientific journals, including the IEEE TRANSACTIONS ON ANTENNAS AND PROPAGATION, IEEE ACCESS, *IET Microwaves, Antennas and Propagation*, *Electronics Letters*, and *The ECTI Transactions on Electrical Engineering, Electronics, and Communications*, and many international conferences, including ISAP and APMC. He was on the Board Committee of ECTI Association, from 2008 to 2011 and from 2014 to 2015. He was an Associate Editor of the *IEICE Transactions on Communications* and the *ECTI Transactions on Electrical Engineering, Electronics, and Communications*. He is also an Associate Editor of the *IEICE Communications Express*.